Surface Defect Engineering in Colored TiO$_2$ Hollow Spheres Toward Efficient Photocatalysis

Letizia Liccardo, Matteo Bordin, Polina M. Sheverdyaeva, Matteo Belli, Paolo Moras, Alberto Vomiero,* and Elisa Moretti*

Nanostructured TiO$_2$ is one of the best materials for photocatalysis, thanks to its high surface area and surface reactivity, but its large energy bandgap (3.2 eV) hinders the use of the entire solar spectrum. Here, it is proposed that defect-engineered nanostructured TiO$_2$ photocatalysts are obtained by hydrogenation strategy to extend its light absorption up to the near-infrared region. It is demonstrated that hydrogenated or colored TiO$_2$ hollow spheres (THS) composed of hierarchically assembled nanoparticles result in much broader exploitation of the solar spectrum (up to 1200 nm) and the engineered surface enhances the photogeneration of charges for photocatalytic processes. In turn, when applied for photodegradation of a targeted drug (Ciprofloxacin) this results in 82% degradation after 6 h under simulated sunlight. Valence band analysis by photoelectron spectroscopy revealed the presence of oxygen vacancies, whose surface density increases with the hydrogenation rate. Thus, a tight correlation between degree of hydrogenation and photocatalytic activity is directly established. Further insight comes from electron paramagnetic resonance, which evidences bulk Ti^{3+} centers only in hydrogenated THS. The results are anticipated to disclose a new path toward highly efficient photocatalytic titania in a series of applications targeting water remediation and solar fuel production.

1. Introduction

The development of efficient, low-cost, and environmentally friendly photocatalysts has attracted the interest of researchers for a series of applications, including production of "green fuels",[1–3] and water remediation from polluting dyes and drugs.[4]

Water contamination is one of the upfront issues to be solved.[5] Complex organic molecules and pharmaceuticals including antibiotics are gaining attention due to their abuse and their low degradability. In fact, antibiotics are largely detected in rivers and water surfaces with concentrations ranging from ng L^{-1} to µg L^{-1}. Hence, their release from wastewater industries is extremely dangerous both for the environment and human health.[6–8] Ciprofloxacin (CIP) is a broad-spectrum second-generation fluoroquinolone antibiotic and one of the most widely used and prescribed. Additionally, it has been proved that CIP is not only present in different water effluents all over the world, but it is also exceeding the safe concentration limit for antimicrobial resistance in several sites.[9] Unfortunately, most wastewater treatment plants are not suitable to eliminate pollutants effectively, so it is extremely important to look for new treatment strategies.

In this regard, photocatalytic advanced oxidation processes (AOPs), such as heterogeneous catalysis, seem to be promising to accelerate the oxidation and degradation of a wide range of organic pollutants. In fact, AOPs use the ability of semiconductor materials to interact with light and to create excitons, whose dissociation induces the formation of electron-hole pairs (e$^-$–h$^+$) that can degrade pollutant molecules via a radical mechanism, thus promoting their mineralization. The production of photogenerated e$^-$–h$^+$ is one of the crucial steps, thus boosting their creation and avoiding fast charge recombination is essential to have high photocatalytic activity.[10] This process requires the presence of an efficient and stable catalyst with a suitable bandgap, able to absorb as much solar light as possible.

Titania (TiO$_2$) is one of the most used photoactive materials, being at the same time non-toxic and cheap. However, its bandgap energy is in the range of 3.0–3.2 eV, so it can absorb light only in the ultraviolet (UV) region, which represents 4–5% of the total solar irradiance spectrum.[11,12] In addition,

L. Liccardo, M. Bordin, A. Vomiero, E. Moretti
Department of Molecular Sciences and Nanosystems
Ca' Foscari University of Venice
Via Torino 155 30172, Venezia Mestre, Italy
E-mail: alberto.vomiero@ltu.se; elisa.moretti@unive.it
P. M. Sheverdyaeva, P. Moras
Istituto di Struttura della Materia-CNR (ISM-CNR)
SS 14, Km 163.5 34149, Trieste, Italy
M. Belli
CNR-IMM
Unit of Agrate Brianza
Via C. Olivetti 2 20864, Agrate Brianza, Italy
A. Vomiero
Division of Materials Science
Department of Engineering Sciences and Mathematics
Luleå University of Technology
97187 Luleå, Sweden

The ORCID identification number(s) for the author(s) of this article can be found under https://doi.org/10.1002/adfm.202212486.

small titania nanoparticles, both in solution or assembled as mesoporous layers, are unable to scatter the impinging light and force it within a confined space, to increase the absorption probability. The development of low-energy gap systems able to confine and absorb light is still a challenge.

Hydrogenated titania is a sub-stoichiometric oxide (TiO_{2-x}), also called colored titania due to the very different colors it can assume (blue, gray, black). It is one of the best sunlight harvesters, as it can absorb light from the UV to the infrared (IR) region of the solar spectrum. Moreover, it has been demonstrated that the oxygen-vacancy-rich black TiO_2 has enhanced photoactivity in several oxidation reactions under visible light as compared to white (stoichiometric) TiO_2.[13,14] Suitable combinations of chemical structure and morphology can further enhance the photochemical activity of a nanostructured system,[15,16] since the functionality of a material can be strongly influenced by its shape and size.

An interesting architecture is represented by hierarchical structures, where small building blocks are assembled into more complex geometries. TiO_2 hollow spheres composed of self-assembled nanoparticles have been successfully applied as decently efficient photocatalysts, by combining the high surface area, and strong light scattering, which induces the light confinement within a small volume, thus increasing the absorption probability.[17,18] However, even the hierarchically assembled white titania hollow spheres suffer from very limited light absorption, due to the large bandgap of the material.

In the present work, colored TiO_2 hollow spheres (THSs), composed of hierarchically assembled nanoparticles, were synthesized by a hard template-based method (see **Figure 1**a), followed by chemical reduction under controlled conditions. Electron paramagnetic resonance (EPR) is used to monitor the presence of defects (Ti^{3+} centers and oxygen vacancies) in the bulk of the materials.[19] X-ray photoelectron spectroscopy (XPS) shows that the density of surface oxygen vacancies increases in a controllable fashion at every step of preparation of the THSs. Their catalytic activity was evaluated by monitoring the photodegradation at room temperature and atmospheric pressure (P_{atm}) of CIP (target molecule), under simulated solar light. We demonstrated that the hydrogenation content, related to the presence of oxygen vacancies, is responsible for the increase in the optical absorption capability of the catalysts (up to the near-IR, NIR, region) thus enhancing the overall photocatalytic efficiency for the investigated photocatalytic oxidation process. We anticipate our results to disclose a new path toward highly efficient photocatalytic titania in a series of applications targeting water remediation and solar fuel production.

2. Results and Discussion

### 2.1. Morphological and Structural Characterization

The surface morphology of THSs samples was analyzed using Field-emission scanning electron microscope (FESEM) (Figure S1, Supporting Information). Poly(methyl methacrylate) (PMMA) nanoparticles exhibited spherical shapes and uniform sizes with an average diameter of 300 nm. No agglomerated nanoparticles were observed. Figure S1 (Supporting

Information) also reports white THS and the gray THS series, after the removal of PMMA through the calcination process. THSs were uniform in size, with diameters ranging from 350 to 400 nm. It is worth mentioning that samples were labeled as X_THSn, where X is referred to the color of the sample: W (white), G (gray), DG (dark gray) and n is the chemical vapor deposition (CVD)-annealing time when it is not 60 min.

The shell thickness was estimated to be ≈50 nm with a relatively rough surface. The appearance of some broken spheres revealed the presence of a void inside, thus confirming that hollow structures were obtained. After the chemical reduction treatment under annealing of W_THSs, no relevant morphological and structural changes were detected. The crystal structure and phase identification were studied through X-ray diffraction (XRD) (Figure S1, Supporting Information). All the THSs samples showed the characteristic peaks of the anatase phase at 2θ values 25.3°, 36.9°, 37.8°, 38.6°, 48.1°, 53.9°, 55.1°, and 62.7°, in agreement with the JCPDS (Joint Committee on Powder Diffraction Standards) card number 21–1272. The anatase crystalline structure has been preserved during the reduction process in all the colored samples, as confirmed by XRD (Figure S1, Supporting Information) and high-resolution transmission electron microscope (HRTEM) analysis (Figure 1b–g). From the HRTEM analysis, the grain size distribution of W_THSs is (9.4 ± 2.9) nm (Figure S2, Supporting Information). Lattice fringes are clearly visible in the polycrystalline structure of Figure 1c. The Selected Area Electron Diffraction (SAED) pattern (Figure 1d) revealed concentric circles, due to the polycrystallinity of THSs samples. The lattice spacing and the crystal phase agree with the results from XRD. The energy dispersive X-ray spectroscopy (EDS) analysis indicates that only Ti and O species can be detected in the W_THS selected sample (Figure 1e–g). The hollow shape was maintained during all the processing steps, including hydrogenation (Figure S1, Supporting Information).

2.2. Optical Characterization

All the diffuse reflectance UV–visible–near-infrared (DRUV-vis-NIR) spectra in **Figure 2**a are characterized by the main absorption feature related to the optical bandgap, which induces the strong absorption edge ≈390 nm (≈3.1 eV). The spectrum for W_THS demonstrates the effectiveness of the hollow sphere,[17] leading to a flat reflectivity below 75% in the full range of 390–1200 nm. Hydrogenation induces the onset of an additional broad absorption band from 500 nm up to (at least) 1200 nm, which is not present in the W_THS sample, whose intensity increases with increasing the wavelengths and the degree of hydrogenation. The light absorption in the vis–NIR region can be enhanced thanks to the disordered surface layer and the presence of surface defects (i.e., oxygen vacancies) generated by hydrogenation.[17,20,21] Our results reveal that the combination of a suitable morphology and the hydrogenation treatment enhanced light absorption in a broad spectral range. The onset of the absorption feature in the low-energy spectral region (>500 nm) may be explained by the presence of localized states below the TiO_2 conduction band (CB) minimum, introduced by the oxygen vacancies, as confirmed by both XPS and EPR analyses (see sections below).[22]
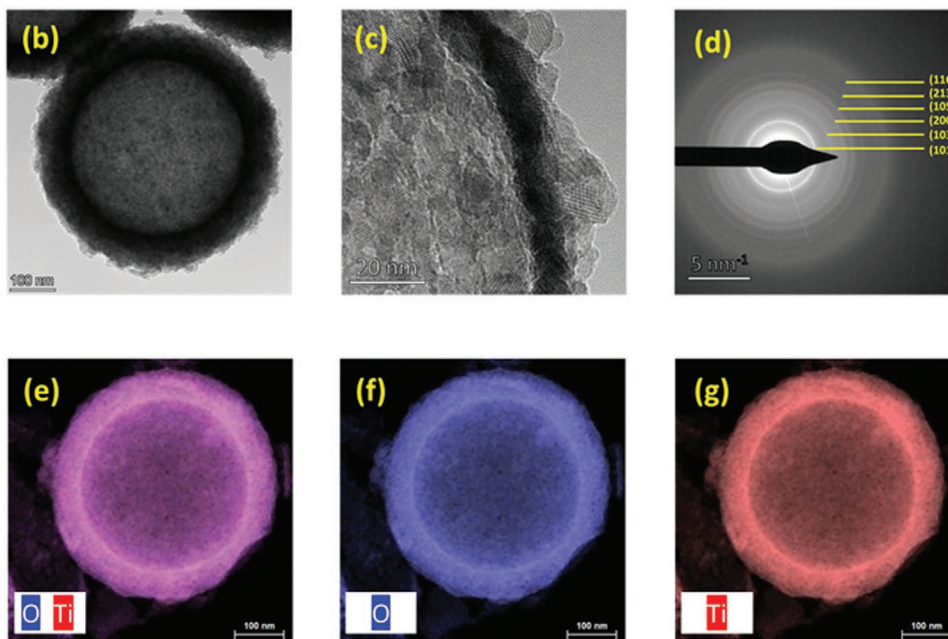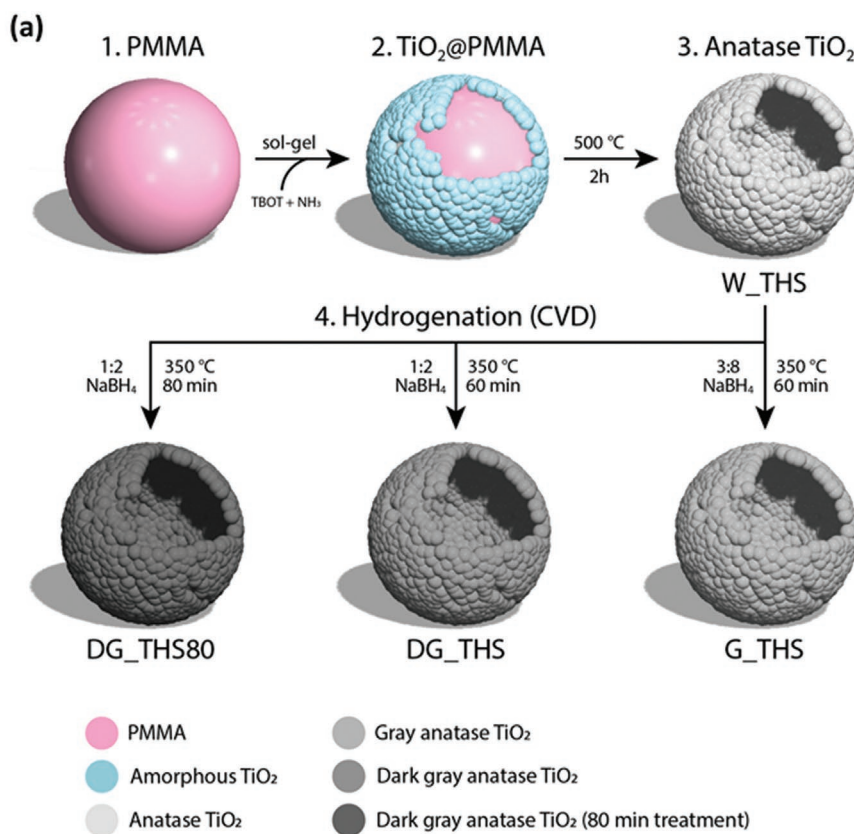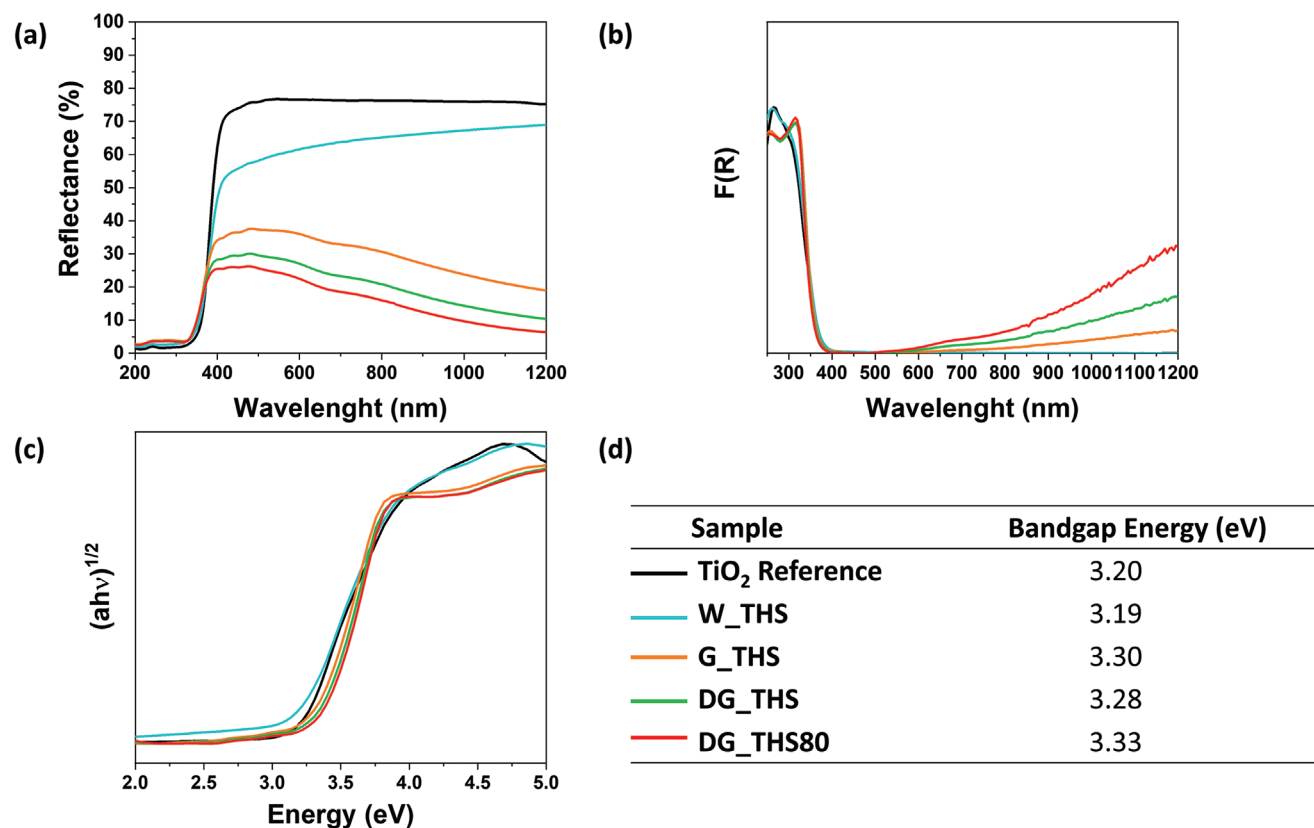
Figure 1. a) Synthesis scheme and b–g) HRTEM analysis of the W_THS sample. b,c) HRTEM images at different magnifications. d) SAED pattern with Miller indexes. e–g) EDS images showing the presence of Ti and O only.

2.3. Photoelectron Spectroscopy Analysis

The electronic structure of the four types of hollow spheres was analyzed by X-ray photoelectron spectroscopy (XPS). The survey spectra (Figure S3, Supporting Information) show the attenuation of the titania-related peaks along the sequence of the CVD preparation steps (Figure 1a), due to the gradual formation of a graphitic coating. Four peaks are necessary to describe the O1s
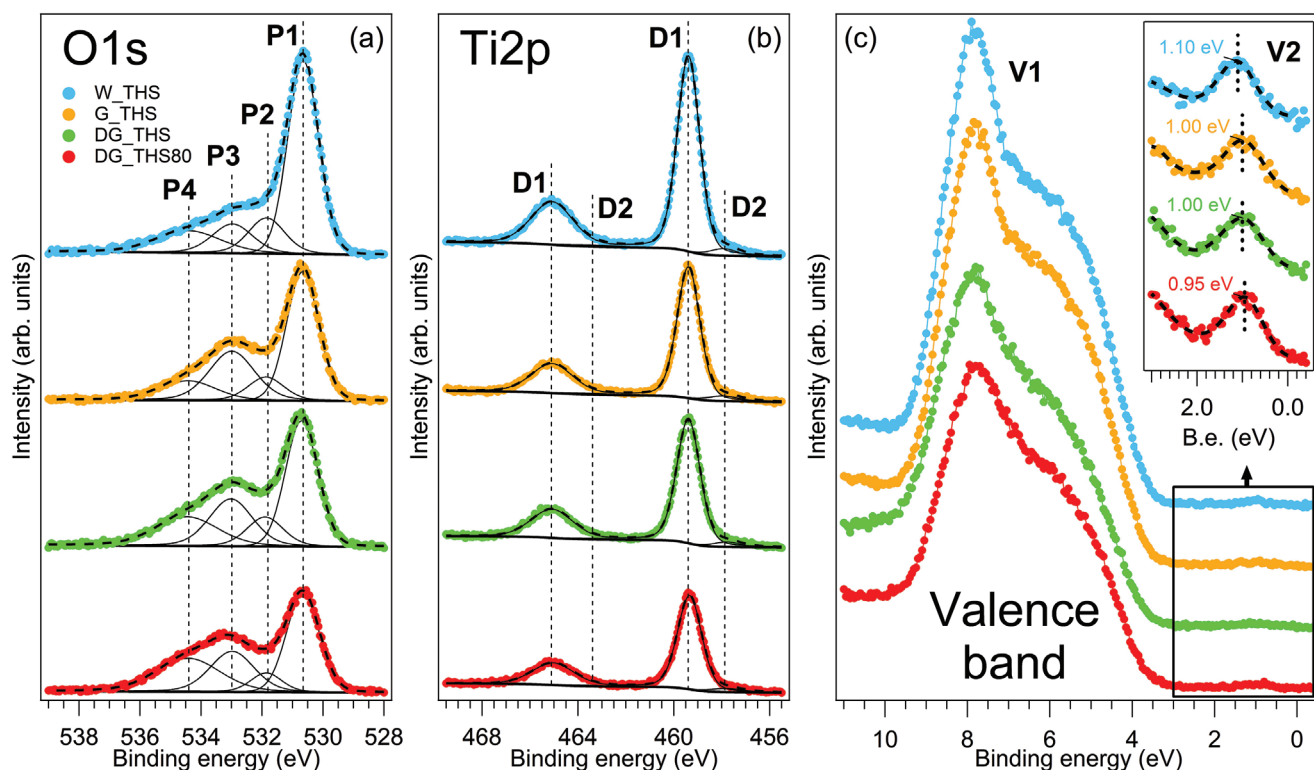
ADVANCED
SCIENCE NEWS
www.advancedsciencenews.com

ADVANCED
FUNCTIONAL
MATERIALS
www.afm-journal.de

Figure 2. a) DRUV–Vis-NIR spectra, b) F(R) spectra calculated through Kubelka–Munk functions, c) Tauc Plots and d) bandgap energies comparison for all the samples, including the TiO_2 Reference.

spectra (**Figure 3**a, photon energy 750 eV). P1 at 530.65 eV and P2 at 531.85 eV are attributed to O in stoichiometric TiO_2 (O_2^-) and OH groups adsorbed on the surface of the THSs. Their ratio remains stable for all THSs (**Table 1**). P3 at 533.0 eV and P4 at 534.4 eV can be associated with C−O and C−OH groups, respectively,[23] and with the presence of adsorbed H_2O.[24] The increasing P3/P1 and P4/P1 ratios along the sequence of CVD cycles (Table 1) can indicate that reduced graphene oxide forms in parallel with the graphitic coating, as suggested by the Fourier Transform Infrared Spectroscopy (FT-IR) spectroscopy data of Figure S4 (Supporting Information). In addition, a higher water content can be ascribed to higher surface concentration of oxygen vacancies which tend to bind water. The Ti2p spectra are very similar for all samples (Figure 3b, with photon energy of 750 eV). They can be fitted with two doublets: the main doublet (D1) at high binding energy derives from Ti in stoichiometric TiO_2 (Ti^{4+}), while the minor doublet (D2) is due to Ti^{3+} defects that probably form during the thermal treatment at 500 °C (step 2 of Figure 1a).[25] The nearly constant D2/D1 ratio (4.2–5.3%, Table 1) shows that the surface concentration of Ti^{3+} is negligibly modified by the CVD preparation procedures at lower temperature (350 °C), which strongly affect the bulk concentration of Ti^{3+} (see Section 2.5). The P1/D1 ratio, normalized to the respective photoemission cross sections at 750 eV (0.24 for O1s and 0.7 for Ti2p),[26,27] is always very close to 2 (Table 1), as expected for stoichiometric TiO_2. The valence band analysis was carried out using resonant conditions (photon

energy 469 eV) in order to probe the defect states (oxygen vacancies and Ti^{3+}) within the gap of stoichiometric TiO_2 with highest sensitivity. In Figure 3c the valence band spectra display strong O2p-related states between ≈3 and 10 eV (V1) and a low-intensity Ti3d-derived state at ≈1 eV (V2), which is better visualized in the inset. The binding energy of V2 shifts continuously from 1.10 to 0.95 eV from W_THS to DG_THS80, i.e., closer to the CB minimum. The V2/V1 ratio can be used to estimate the concentration of the defects in the near-surface region of the samples. As the concentration of the Ti^{3+} defects remains stable (Figure 3b), the higher V2/V1 ratio reflects the increasing concentration of oxygen vacancies with the CVD treatments (Table 1).

2.4. FT-IR Spectroscopy

Figure S4a (Supporting Information) shows the FT-IR spectra of W_THS, DG_THS, and DG_THS80. The titania characteristic absorption bands are the Ti−O−Ti symmetrical stretching at 686 cm^{-1} and the Ti−O vibration band located at 505 cm^{-1}.[28] The broad band at ≈3500 cm^{-1} corresponds to the stretching vibrations of OH groups.[29] Furthermore, the band located at 1631 cm^{-1} can be attributed to the combination of Ti−OH bending due to the H_2O molecules adsorbed on the sample's surface and to the C=C stretching vibration that can be associated with the presence of graphitic carbon. The band at

**ADVANCED
SCIENCE NEWS**

www.advancedsciencenews.com

**ADVANCED
FUNCTIONAL
MATERIALS**

www.afm-journal.de

Figure 3. XPS characterization of the THSs. The spectra were collected at photon energy 750 eV for the a) O1s and b) Ti2p core levels and photon energy 468 eV for the c) valence band. The inset in panel (c) shows a zoom of the fundamental gap region of the THSs, where defect states (V2) are detected.

1570 cm⁻¹ is attributed to the presence of aromatic C=C vibrations and the band at 1360 cm⁻¹ to C−OH stretching, leading to the conclusion that there is the presence of graphitic carbon and graphene oxide on the surface of the hydrogenated samples.[28,30] These results are consistent with XPS analysis. Figure S4b (Supporting Information) shows the FT-IR spectra for the bare (W_THS) and the hydrogenated samples after and before the CIP photodegradation experiments, labeled as DG_THS, DG_THS80, and DG_THS photodeg, DG_THS80 photodeg, respectively. Slight differences can be detected between the spectra before and after the photocatalytic experiments. The main difference found in the used samples is the presence of two low-intensity bands located at ≈2850 and 2910 cm⁻¹ associated to aromatic and aliphatic C−H stretching of CIP functional groups, which indicates that only a few of CIP molecules are adsorbed onto the surface of the photocatalysts.[30]

Table 1. Numerical values derived from the XPS data (shown in Figure 3).

Sample	W_THS	G_THS	DG_THS	DG_THS80
P2/P1 [%]	24	23	28	20
P3/P1 [%]	22	59	55	60
P4/P1 [%]	26	28	48	71
D2/D1 [%]	4.2	5.3	4.5	5.1
P1/D1	2.03	2.05	2.08	2.14
V2 binding energy [eV]	1.10	1.00	1.00	0.95
V2/V1 [%]	1.7	1.8	2.7	3.0

2.5. EPR Spectroscopy

Figure 4 shows the room temperature EPR spectra of THS with different degrees of hydrogenation in the $g = 2$ region. Data are reported after the removal of a parabolic background and the normalization to the maximum of each spectrum, to better appreciate its features.

W_THS shows a single transition, characterized by a small anisotropy, almost unobservable because of the signal line width ($g_\perp = 2.0021$, $g_\parallel = 2.0007$, Gaussian and Lorentzian peak-to-peak widths σ_{pp} and λ_{pp} of 0.22 and 0.17 mT respectively). This center is generally ascribed to oxygen vacancies (OV), though we observe a g factor slightly shifted to lower values with respect to the literature ($g = 2.002–2.003$).[19,25] Following hydrogenation, the OV signal is still present though with parameters closer to the expected values ($g_\perp = 2.0026$, $g_\parallel = 2.0016$, $\sigma_{pp} = 0.64$, $\lambda_{pp} = 0.38$). Moreover, three other centers emerge: a broader transitions at higher magnetic field values ($g_\perp = 1.988$, $g_\parallel = 1.978$, $\sigma_{pp} = 0.2$, $\lambda_{pp} = 1.2$); another weak center at intermediate g factor which is responsible for the strange asymmetric line shape of the OV center in the treated material ($g_\perp = 2.0004$, $g_\parallel = 1.9935$, $\sigma_{pp} = 0.54$, $\lambda_{pp} = 0.04$); an extremely broad peak (peak-to-peak width higher than 110 mT) centered around $g = 2.4–2.45$ (Figure S9, Supporting Information). The first center is generally attributed to paramagnetic Ti³⁺ centers.[19,25] The fact that no such signal is observed in W_THS while, for the same material, Ti³⁺ is observed by XPS may be related to the different parts of the sample the two techniques probe. If hydrogenation promotes the formation of Ti³⁺ at the surface
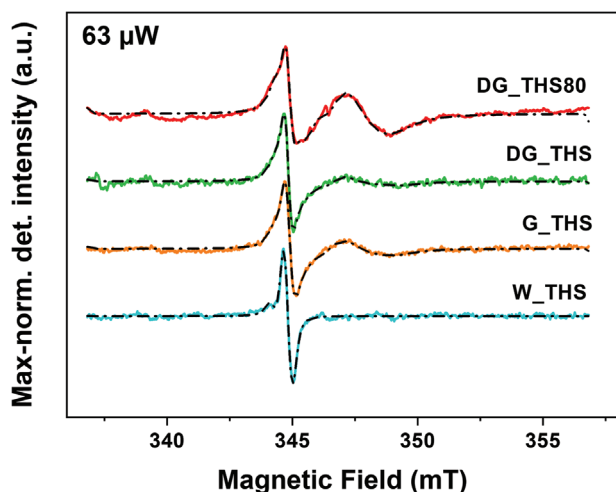
Figure 4. Stacked EPR spectra of THS with different degrees of hydrogenation. The applied power was selected not to saturate any of the signals. Ordinate scale represents data after the subtraction of a parabolic background, and normalization to the maximum value in each spectrum, to better visualize the relative weight of the various components. Fitting curves of the single spectra are also included (black dash-dot line) and the corresponding spin-Hamiltonian parameters can be found in (Figures S5–S9 and Tables S1–S4, Supporting Information).

and their diffusion into the bulk portion of the THS, Ti^{3+} centers too weak to be recorded by EPR in the pristine material may become observable. The interpretation of the second center is not straightforward. Despite the fact that it is present only together with the Ti^{3+} center, it does not fall in the typical g factor range of Ti^{3+} centers.[31–33] It is more probably a carbon-related center, possibly interacting with Ti^{3+} centers nearby. This attribution is suggested in the literature[34] and would be compatible with XPS characterization. Low-temperature EPR characterization may help to unravel this issue. The last center is responsible for the large negative background overlapping the g = 2 region. Such a background can be observed in various reports, but it is not often commented on. Its width and placement suggest that it is likely due to ferromagnetic resonance from magnetic impurities, which can give very large signals at unusual g factor values even if in trace amounts. This effect is due to the enhancement inherent in their intrinsic magnetization. Similar signals were observed in TiO_2 samples after 2 h ball milling, for example.[35] Presumably, it is not due to Fe contaminants, nor to ferromagnetic interactions between Ti^{3+} centers, which would both introduce well-defined features in a different g range, at least for a substitutional fraction.[31,36,37]

The intensity ratio of the Ti^{3+} component with respect to the OV component for G_THS, DG_THS, and DG_THS80 is roughly 1.5, 1.2, and 3.9, respectively, while it is identically 0 for W_THS which does not show Ti^{3+} even at large microwave power. The ratio of the C-related component with respect to the OV component is 0, 0.2, 0.3, and 0.4. for W_THS, G_THS, DG_THS, DG_THS80 respectively.

2.6. Photodegradation of Ciprofloxacin under Simulated Solar Light

The photocatalytic activity of all THS samples was evaluated under simulated solar light irradiation, in an aqueous solution

and at room temperature (**Figure 5**a,b). In all cases, we monitored for 360 min the typical CIP main absorbance peak located at ≈273 nm. The photolysis of the base CIP was used as a reference (black curves). Figure 5a shows the photocatalytic degradation of CIP with and without catalysts in terms of the concentration of CIP C at a given exposure time with respect to its initial value C_0 at −60 min (60 min is the equilibration time before the exposure to the solar light). The C/C_0 curve of bare CIP decreases slightly (≈13%) over 360 min, thus confirming the substantial stability of CIP under sunlight irradiation. After 60 min of equilibration in the dark in the presence of TiO_2 Reference and THS samples, CIP is partially adsorbed on the surface of the photocatalysts, from 2% for W_THS to 20% for DG_THS80 and 30% for TiO_2 Reference. The efficiency of the photocatalytic degradation is known to depend crucially on the type of the adsorption phenomena involved, which are also affected by the pH of the solution. Indeed, the solution pH influences both the charge of the photocatalyst surface and the drug molecules as well as their possible interactions. The zero-point charge (pH_{zpc}) is defined as the pH at which the catalyst surface is uncharged. According to the literature, pH_{zpc} for stoichiometric TiO_2 is between 5 and 6. In addition, CIP shows different pKa associated to its functional groups and can take different charges according to the pH of the solution.[27,38] In general, in alkali conditions CIP is predominantly in its anionic form, on the contrary in cationic form in acidic conditions. Hence, in water at a neutral pH CIP is in its zwitterionic form so that it will interact weakly with the pure TiO_2 photocatalyst surface. When the hydrogenation content increases, the pH_{zpc} of the colored TiO_2 changes. In detail, values reported in literature are below the neutral pH, thus the hydrogenated particle suspensions in water (pH = 7) are stabilized by repulsive forces coming from their negatively charged surface. Oxygen vacancies may lead to an increase in the adsorption of water molecules thus hydroxylating the catalyst's surface, affecting the adsorption of CIP molecules and the overall degradation pathway.[39,40] This mechanism explains the marked decrease of C/C_0 as a function of the exposure time when THS samples were added to the solution.

For comparison purposes, a commercial white titania (pure anatase polymorph, as the THS samples) was also investigated under the same reaction conditions. All the synthesized samples showed excellent and improved photocatalytic activity with respect to the commercial TiO_2 Reference, which can degrade CIP only at 61%. The best-performing sample is G_THS, which degrades 82% of CIP within 360 min and presents a kinetic constant of 11.9 10^{-3} min^{-1} (the kinetic constants for all the samples are reported in Figure 5b,c). Interestingly, the high hydrogenation content of DG_THS80 is accompanied by lower photocatalytic activity among the colored samples. When dealing with hydrogenated TiO_2, the correlation between the physicochemical properties and the photocatalytic performances is complicated and often results in conflicting results.[22] In our case, XPS and EPR analysis confirmed the presence of surface defects such as Ti^{3+} centers and oxygen vacancies, which are highly visible in DG_THS80. The role of the oxygen vacancies and Ti^{3+} centers have been widely discussed in the literature and their concentration has an impact on the photocatalytic activity.[41,42] In fact, defects act as recombination centers for photogenerated electron-hole pairs and cause a decrease in the
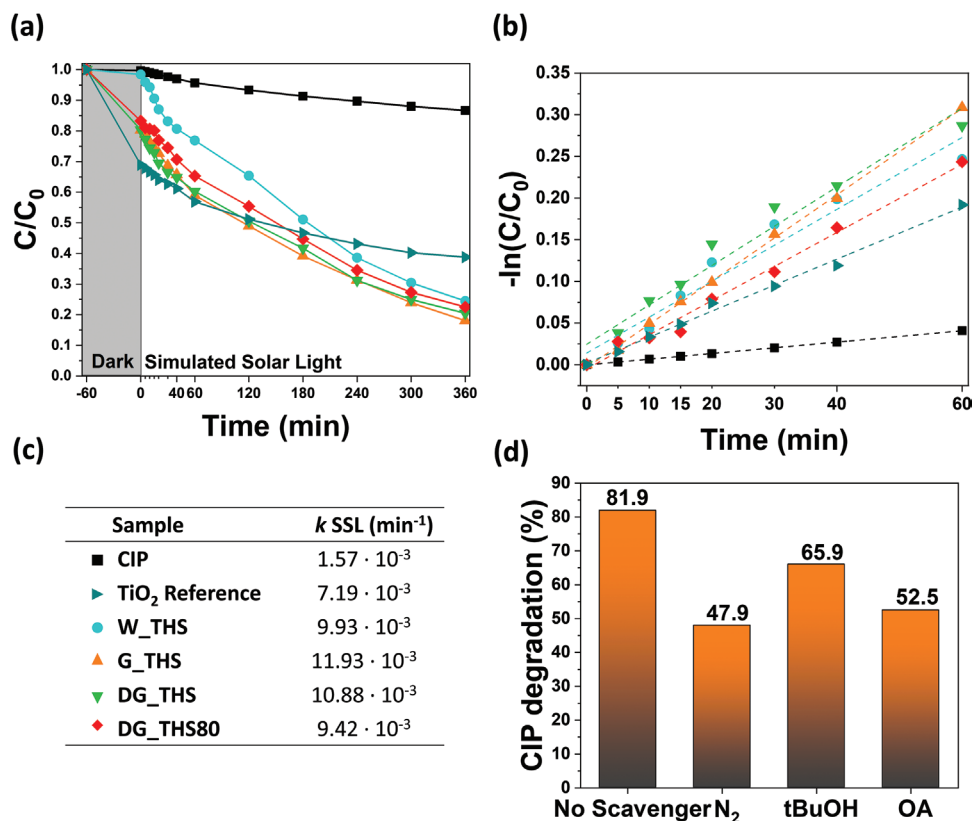
Figure 5. a) Photocatalytic degradation of CIP as a function of irradiation time with and without catalysts (CIP curve) under simulated solar light irradiation. b) CIP degradation kinetics with linear fits of the experimental data in dashed lines. c) Legend and kinetic constant values for all the samples under simulated solar light (SSL). d) Scavenger experiments of the active species for the degradation of CIP in presence of G_THS.

overall photocatalytic efficiency. However, the same Ti^{3+} sites and oxygen vacancies have been shown to be responsible for the increasing ability in absorbing a broader range of wavelengths up to the NIR region. Consequently, a trade-off between light absorption and catalytic activity is needed to maximize the photocatalysis. G_THS showed the lowest amount of surface defects. This feature prevents charge-carriers recombination, thus lowering the electrons trapping phenomena and promoting the conversion of oxygen molecules into superoxide radicals, necessary for CIP photodegradation.[43]

Another important point deserves to be discussed: the role of graphitic carbon on the photocatalytic properties. The combination of XPS and FT-IR analysis may help on the matter. In fact, XPS highlights the formation of graphitic coating along the sequence of the CVD preparation steps. The presence of carbon coating is also confirmed by FT-IR analysis of the samples DG_THS and DG_THS80 before the catalytic tests: the samples DG_THS and DG_THS80 clearly present the two FT-IR absorption bands at 1570 and 1360 cm^{-1}, which are not present in the sample W_THS. After the first cycle of photocatalysis, the FT-IR analysis was repeated (Figure S4, Supporting Information) and the two bands at 1570 and 1360 cm^{-1} disappeared. After three catalytic cycles, we also repeated the XPS measurement on sample DG_THS (Figure S10, Supporting Information), which indicated a drastic decrease in the surface graphitic carbon content. The experimental evidence from both FT-IR and XPS indicates strong reduction of graphitic carbon content

in the DG sample series after the photocatalytic tests. Despite the strong modification of carbon content, the functional tests of Figure S11 (Supporting Information) demonstrate no variation in the photocatalytic activity during cycles 1, 2, and 3 of the reusability test. The combination of these data allows us to conclude that the surface graphitic carbon plays a negligible role in the functional properties of the material and tends to disappear during the re-use of the colored hollow spheres.

Since the peculiarity of the hydrogenated THSs is the broad absorbance in the visible region, we also evaluated the photocatalytic activity of the best-performing sample (i.e., G_THS) under both UV and vis light, in the same conditions used before, to compare the obtained results and examine wavelength dependence. As expected, G_THS photocatalyst is active both under UV and vis light, showing a CIP degradation of 98% and 54%, respectively, after 180 min of irradiation time (Figure S12, Supporting Information).

Stability and reusability test of the best-performing photocatalyst (G_THS), was carried out (Figure S11, Supporting Information). A slightly increased photocatalytic activity (+5%) was observed soon after the first-cycle test. Simultaneously, a decrease of the CIP adsorption process from 20% of adsorbed species during the first cycle to 11% during the third cycle in the dark period was recorded. This behavior can be attributed to the adsorption of degradation by-products on the active sites which leads, at the same time, to faster production of radicals. Finally, free radical trapping experiments were conducted to

ADVANCED
SCIENCE NEWS

www.advancedsciencenews.com

ADVANCED
FUNCTIONAL
MATERIALS

www.afm-journal.de

investigate the main active species responsible for CIP degradation (Figure 5d). The photocatalytic efficiency of G_THS is significantly inhibited when N_2 (O_2^- scavenger) and OA (h^+ scavenger) are introduced into the system, while barely affected upon the addition of tBuOH (OH scavenger). Hence, superoxide radicals (O_2^-) and holes (h^+) should be the two major reactive species involved in the CIP degradation by G_THS under simulated solar light irradiation.

3. Conclusions

We have proposed an easy and cost-effective way to obtain hydrogenated and colored THS composed of hierarchically assembled nanoparticles as promising photocatalysts for water remediation. The hollow microstructures, in combination with the defect-engineered surface, enable the exploitation of solar light in a much broader spectral range (200–1200 nm), compared to the bare titania counterpart. We recorded highly effective exploitation of photogenerated charges in photocatalytic degradation of the well-known water contaminant CIP. The best-performing sample reached 82% of degradation efficiency under simulated solar light irradiation at room temperature and atmospheric pressure. We showed that the hydrogenation degree, related to the presence of oxygen vacancies on the catalyst's surface, seems to lead to an increase in the optical absorption and the overall photocatalytic activity of the samples. We showed also that hydrogenation undoubtedly introduces defects that are not present in pristine THS, as monitored by magnetic resonance. Benefitting from the design, the recorded functionality, and the understanding of physico-chemical properties of these materials, colored THS may offer a promising strategy to obtain novel and efficient photocatalysts. Therefore, this work provides inspiration to produce a cheap, environmentally friendly, stable, and efficient photocatalyst, which holds a great potential for the development of new technologies not only for water remediation applications but also for energy applications in the field of solar fuel production.

4. Experimental Section

Materials: The following commercial reagents, without any further purification, were used in all the experimental phases: milli-Q water (H_2O); nitrogen gas (N_2); methyl methacrylate (MMA, Merck ≥ 99.0%); 2,2'-azobis (2-methylpropionamidine) dihydrochloride (azobis, Merck 97%); deionized water (H_2O); ethanol absolute (EtOH, Merck ≥ 99.5%); titanium(IV) butoxide (TBOT, Merck 97%); ammonia solution 28%w (NH_3, Merck ≥ 99.9%); sodium borohydride ($NaBH_4$, Merck ≥ 98%); argon (Ar, Merck ≥ 99.998%); methylene blue (MB, Merck ≥ 82%); CIP (CIP, Merck ≥ 98%); Titanium(IV) oxide (TiO_2 Reference, Anatase, Merck ≥ 99.5%).

Synthesis of White TiO_2 Hollow Spheres: The synthesis of white TiO_2 hollow (W_THS) spheres involved a hard template-based approach. The first step was the synthesis of PMMA templating spheres. Briefly, MMA (12.5 wt.%) was dispersed in Milli-Q water under vigorous magnetic stirring (700 rpm), bubbling N_2 (g). Subsequently, the mixture was heated up to 80 °C and the azobis initiator (0.19 wt.%) was added. The reaction was carried out for 2 h, producing colloidal PMMA spheres. The reaction was rapidly stopped by cooling in an ice bath and the resulting PMMA spheres were separated by centrifugation (4000 rpm for 25 min).

They were washed with deionized water and ethanol repeatedly. Finally, the product was dried in the air overnight.

The second step involved the coating of the sacrificial template using a titanium precursor to obtain a TiO_2@PMMA core-shell system. Specifically, 1 wt.% PMMA spheres were dispersed in absolute ethanol and sonicated for 20 min. The system was heated to 45 °C and stirred at 500 rpm. 0.1 wt.% of the ammonia solution and 1.5 wt.% TBOT were added, and the reaction was carried out for 24 h. The resulting product was collected by centrifugation and washed with deionized water and ethanol several times.

The removal of PMMA-templates and the calcination process are the last steps to produce THSs. In detail, the core-shell spheres were thermally treated at 500 °C for 2 h (ramp rate 2 °C min^{-1}) in airflow and W_THSs were obtained.

Synthesis of Colored TiO_2 Hollow Spheres: To obtain colored THSs, W_THS and $NaBH_4$ were mixed in different ratios and grounded for 20 min thoroughly. Then, the product was placed in a tubular furnace, ready for the chemical vapor deposition (CVD) technique. Inside the CVD, the powder was thermally treated at 350 °C under Ar atmosphere (flow rate 150 sccm) for 60 or 80 min (heating rate 10°C min^{-1}), according to the desired samples. After cooling to room temperature, the colored THSs were accurately rinsed several times with deionized water and ethanol to remove unreacted $NaBH_4$, and finally dried at 70 °C overnight. Samples were labeled as X_THSn, where X was referred to the color of the sample: W (white), G (gray), DG (dark gray) and n was the CVD-annealing time when it was not 60 min.

G_THSs were obtained using a weight ratio between $NaBH_4$ and W_THS of 3 to 8, respectively, and a 60 min CVD-annealing time. DG_THS and DG_THS80 samples were synthesized through the same operating conditions but using a weight ratio between $NaBH_4$ and W_THS of 1 to 2 and, in the case of DG_THS80 a CVD-annealing time of 80 min.

Characterization Techniques: Field-emission scanning electron microscopy (FESEM) was performed with Zeiss SUPRA 40 instruments. All micrographs were taken at a 5 kV electron gun accelerating voltage. High-resolution transmission electron microscopy (HRTEM), and energy dispersive X-ray analysis (EDX) elemental mapping were carried out on a FEI Talos F200S scanning/transmission electron microscope (S/TEM) at an acceleration voltage of 200 kV. The average grain size distribution was determined by grain size analysis software evaluation. The X-ray diffraction (XRD) analyses were carried out with PanAlytical Empyrean XRD, equipped with Cu kα radiation. The scan rate was 2°min^{-1}. X-Ray diffraction patterns were collected in the range 10–80 2θ degrees. For sample identification, diffraction patterns were matched to the JCPDS database.

Fourier Transform Infrared Spectroscopy (FT-IR) was led using a Perkin-Elmer Spectrum 1000 spectrometer equipped with a Platinum Diamond attenuated total reflectance (ATR). FT-IR spectra were collected in the range 4000–400 cm^{-1}.

UV–is-NIR diffuse reflectance (DRUV-vis-NIR) spectra were collected with a Perkin Elmer Lambda 1050+ UV–vis-NIR spectrophotometer, equipped with an integrating sphere, for wavelengths ranging from 200 to 1200 nm. The bandgap (E_g) was determined using the Kubelka–Munk approach (Equation 1).[44]

$$F(R_\infty) = \frac{(1 - R_\infty)^2}{2R_\infty} = \frac{K}{S} \tag{1}$$

Here, $F(R_\infty)$ is the Kubelka–Munk function, R_∞ is the diffuse reflectance, K is the absorption coefficient, and S is the scattering coefficient. Then by exploiting the Tauc method,[45] the bandgap for TiO_2 semiconductors can be expressed using the following equation Equation 2:

$$\left(F(R_\infty)h\nu\right)^{\frac{1}{2}} = B\left(h\nu - E_g\right) \tag{2}$$

Here, h is the Planck's constant, ν is the frequency of the light and B is a constant. By plotting $F(R_\infty)$ versus the energy expressed in eV, and

by finding the x-axis intersection point of the linear fit of the Tauc plot, it is possible to estimate the bandgap of a material.[45]

The XPS measurements were carried out at the VUV-Photoemission beamline of the synchrotron Elettra (Trieste, Italy).

Electron paramagnetic resonance investigations were performed with a Bruker Elexsys E580 instrument equipped with a standard X-band cylindrical cavity (ER-4118X-MD5). The powder samples were introduced in fused quartz EPR tubes. g factor values around $g = 2$ were calibrated with an α-α'-diphenyl-β-picryl-hydrazyl (DPPH) standard ($g = 2.0036 \pm 0.0003$), while for the large scan in Figure S9 (Supporting Information), the applied correction consisted in a linear extrapolation of the $g = 2$ correction and no correction at zero magnetic fields. Analysis routines made use of the EASYSPIN software for MATLAB^{TM}.[46] In particular, a first-stage analysis introducing background, OV, and Ti^{3+} centered in the fitting model showed structured residuals for all hydrogenated samples, in the form of an axially symmetric powder pattern which was thus introduced into the model. Experimental issues did not allow to extract the spin concentration of the different samples in the spectra, though relative quantitative considerations could be performed and are described in the main text and in the Supporting Information.

Photocatalytic Tests: The degradation of ciprofloxacin (CIP), an antibiotic, was chosen as a test reaction to evaluate the photocatalytic activity of the synthesized materials under solar simulated light and both UV and visible (vis) light irradiation to evaluate wavelength dependences of photocatalytic activity at several different wavelengths. The UV and vis photocatalysis reactions took place in a reactor system, where six sets of 6 W UV-B lamps (Sankyo, Japan) for UV irradiation (365 nm) and a 13 W visible sodium lamp (Osram, Germany) for visible light irradiation were used. The main photocatalytic test was carried out under Sunlight Solar Simulator, AM1.5G filter, 100 W Xenon arc lamp (Abet Technologies, USA). During the photocatalysis, the reactor was positioned under the solar lamp at a suitable distance to obtain a power of 1 sun (1350 W m^{-2}). The photon flux was measured by using a Si-based reference solar cell #15 150 (Abet Technologies, USA) leaned against the external wall of the photoreactor containing only pure water. A 100 mL cylindrical concentric Pyrex-quartz photocatalytic reactor was employed. The initial concentration of the target molecule was 2×10^{-5} M and the amount of photocatalyst was fixed at 125 mg L^{-1}. The photodegradation tests were performed at r.t. and P$_{atm}$ and at solution's pH (pH = 5). Prior to irradiation, the solutions were put in dark for 60 min to reach the adsorption equilibrium. At given time intervals, 1 mL of solution was collected from the reactor, filtered through a 0.45 mm PTFE Millipore disc to remove the catalyst powder, and used for successive UV–vis spectroscopy analysis. A Perkin Elmer Lambda 1050+ UV–vis-NIR was used for these measurements. The degradation processes were observed following the maximum of absorbance (273 nm for CIP) in the UV–vis spectrum of the target molecule. Then, once calculated the concentration at this specific wavelength using the Lambert-Beer law, it was possible to calculate the degradation rate $\frac{C}{C_0}$, where C is the concentration after time t and C_0 represents the initial concentration at $t = 0$. Kinetics study involved in the CIP molecules photodegradation was carried out evaluating the data interval from 0 to 60 min and adopting the pseudo-first-order model:

$$ln\frac{C}{C_0} = -kt \tag{3}$$

where k is the pseudo-first-order rate constant (min^{-1}), calculated as

$$k = 2.303 \times slope \tag{4}$$

To evaluate the stability and reusability of the photocatalysts, a 3-cycle recycling test was performed. The best-performing sample was collected by centrifugation, washed with deionized water several times, and dried overnight after each photocatalytic cycle.

The main active species in the CIP degradation were investigated by performing the free radical trapping experiments. Briefly, three different photocatalytic tests were carried out using the same conditions as before but adding to the reaction system tert-Butanol (tBuOH, 1 mM), oxalic acid (OA, 1 mM) and N$_2$ (g) as OH, holes, and O$_2^-$ scavengers, respectively.

Supporting Information

Supporting Information is available from the Wiley Online Library or from the author.

Conflict of Interest

The authors declare no conflict of interest.

Data Availability Statement

The data that support the findings of this study are available from the corresponding author upon reasonable request.

[1] T. A. Shifa, F. Wang, Z. Cheng, P. He, Y. Liu, C. Jiang, Z. Wang, J. He, *Adv. Funct. Mater.* **2018**, *28*, 1800548.

[2] H. Luo, J. Barrio, N. Sunny, A. Li, L. Steier, N. Shah, I. E. L. Stephens, M. Titirici, *Adv. Energy Mater.* **2021**, *11*, 2101180.

[3] H. Zhang, C. Li, C. Lyu, L. Hu, *Appl. Catal. B* **2020**, *270*, 118874.

[4] M. Telkhozhayeva, B. Hirsch, R. Konar, E. Teblum, R. Lavi, M. Weitman, B. Malik, E. Moretti, G. D. Nessim, *Appl. Catal., B* **2022**, *318*, 121872.

[5] E. Moretti, E. Cattaruzza, C. Flora, A. Talon, E. Casini, A. Vomiero, *Appl. Surf. Sci.* **2021**, *553*, 149535.

[6] E. E. Mitsika, C. Christophoridis, N. Kouinoglou, N. Lazaridis, C. K. Zacharis, K. Fytianos, *J. Hazard. Mater.* **2021**, *403*, 123819.

[7] S. Wu, Y. H. Hu, *Chem. Eng. J.* **2021**, *409*, 127739.

[8] C. Alberoni, I. Barroso-Martín, A. Infantes-Molina, E. Rodríguez-Castellón, A. Talon, H. Zhao, S. You, A. Vomiero, E. Moretti, *Mater. Chem. Front.* **2021**, *5*, 4138.

[9] J. L. Wilkinson, A. B. A. Boxall, D. W. Kolpin, K. M. Y. Leung, R. W. S. Lai, D. Wong, R. Ntchantcho, J. Pizarro, J. Mart, S. Echeverr,

**ADVANCED
SCIENCE NEWS**

www.advancedsciencenews.com

**ADVANCED
FUNCTIONAL
MATERIALS**

www.afm-journal.de

J. Garric, A. Chaumot, P. Gibba, I. Kunchulia, S. Seidensticker, G. Lyberatos, J. M. Morales-salda, H. Kang, *Proc. Natl. Acad. Sci. USA* **2022**, *119*, e2113947119.

[10] D. Ma, H. Yi, C. Lai, X. Liu, X. Huo, Z. An, L. Li, Y. Fu, B. Li, M. Zhang, L. Qin, S. Liu, L. Yang, *Chemosphere* **2021**, *275*, 130104.

[11] I. Concina, Z. H. Ibupoto, A. Vomiero, *Adv. Energy Mater.* **2017**, *7*, 1700706.

[12] J. Liu, N. Ma, W. Wu, Q. He, *Chem. Eng. J.* **2020**, *393*, 124719.

[13] L. Jiang, S. Zhou, J. Yang, H. Wang, H. Yu, H. Chen, Y. Zhao, X. Yuan, W. Chu, H. Li, *Adv. Funct. Mater.* **2022**, *32*, 2108977.

[14] X. Liu, G. Zhu, X. Wang, X. Yuan, T. Lin, F. Huang, *Adv. Energy Mater.* **2016**, *6*, 1600452.

[15] J. Xiong, J. Di, J. Xia, W. Zhu, H. Li, *Adv. Funct. Mater.* **2018**, *28*, 1801983.

[16] L. Liccardo, E. Lushaj, L. Dal Compare, E. Moretti, A. Vomiero, *Small Sci.* **2022**, *2*, 2100104.

[17] Y. Wang, J. Cai, M. Wu, H. Zhang, M. Meng, Y. Tian, T. Ding, J. Gong, Z. Jiang, X. Li, *ACS Appl. Mater. Interfaces* **2016**, *8*, 23006.

[18] W. Hu, W. Zhou, K. Zhang, X. Zhang, L. Wang, B. Jiang, G. Tian, D. Zhao, H. Fu, *J. Mater. Chem. A* **2016**, *4*, 7495.

[19] Y. Wang, K. I. Saitow, *Chem. Mater.* **2020**, *32*, 9190.

[20] X. Chen, L. Liu, P. Y. Yu, S. S. Mao, *Science* **2011**, *331*, 746.

[21] T. Xia, Y. Zhang, J. Murowchick, X. Chen, *Catal. Today* **2014**, *225*, 2.

[22] T. S. Rajaraman, S. P. Parikh, V. G. Gandhi, *Chem. Eng. J.* **2020**, *389*, 123918.

[23] B. Gupta, N. Kumar, K. Panda, V. Kanan, S. Joshi, I. Visoly-Fisher, *Sci. Rep.* **2017**, *7*, 45030.

[24] I. Luciu, R. Bartali, N. Laidani, *J. Phys. D* **2012**, *45*, 345302.

[25] X. Pan, M. Q. Yang, X. Fu, N. Zhang, Y. J. Xu, *Nanoscale* **2013**, *5*, 3601.

[26] J. J. Yeh, I. Lindau, *At. Data Nucl. Data Tables* **1985**, *32*, 1.

[27] X. Hu, X. Hu, Q. Peng, L. Zhou, X. Tan, L. Jiang, C. Tang, H. Wang, S. Liu, Y. Wang, Z. Ning, *Chem. Eng. J.* **2020**, *380*, 122366.

[28] D. Liang, C. Cui, H. Hub, Y. Wang, S. Xu, B. Ying, P. Li, B. Lu, H. Shen, *J. Alloys Compd.* **2014**, *582*, 236.

[29] M. M. Kumar, S. Badrinarayanan, M. Sastry, *Thin Solid Films* **2000**, *358*, 122.

[30] S. A. Khan, Z. Arshad, S. Shahid, I. Arshad, K. Rizwan, M. Sher, U. Fatima, *Compos. B Eng.* **2019**, *175*, 107120.

[31] M. Chiesa, S. Livraghi, E. Giamello, E. Albanese, G. Pacchioni, *Angew. Chem.* **2017**, *129*, 2648.

[32] M. Chiesa, M. C. Paganini, S. Livraghi, E. Giamello, *Phys. Chem. Chem. Phys.* **2013**, *15*, 9435.

[33] A. Naldoni, M. Altomare, G. Zoppellaro, N. Liu, Š. Kment, R. Zbořil, P. Schmuki, *ACS Catal.* **2019**, *9*, 345.

[34] I. Caretti, M. Keulemans, S. W. Verbruggen, S. Lenaerts, S. van Doorslaer, *Top. Catal.* **2015**, *58*, 776.

[35] S. Indris, R. Amade, P. Heitjans, M. Finger, A. Haeger, D. Hesse, W. Grünert, A. Börger, K. D. Becker, *J. Phys. Chem. B* **2005**, *109*, 23274.

[36] X. Li, P. L. Yue, C. Kutal, *New J. Chem.* **2003**, *27*, 1264.

[37] A. Yermakov, D. Boukhvalov, M. Uimin, V. Mesilov, A. Minin, V. Galakhov, A. Korolyov, A. Volegov, E. Rosenfeld, A. Gubkin, L. Molochnikov, *J. Phys.: Conf. Ser.* **2019**, *1389*, 012026.

[38] X. Wei, J. Chen, Q. Xie, S. Zhang, L. Ge, X. Qiao, *Environ. Sci. Technol.* **2013**, *47*, 4284.

[39] L. Y. Ozer, H. Apostoleris, F. Ravaux, S. I. Shylin, F. Mamedov, A. Lindblad, F. O. L. Johansson, M. Chiesa, S. Jacinto, G. Palmisano, *ChemCatChem* **2018**, *10*, 2949.

[40] M. Sarafraz, M. M. Amini, A. Adiban, A. Eslami, *Mater. Sci. Semicond. Process.* **2020**, *120*, 9.

[41] X. Wang, L. Mayrhofer, M. Hoefer, S. Estrade, L. Lopez-Conesa, H. Zhou, Y. Lin, F. Peiró, Z. Fan, H. Shen, L. Schaefer, M. Moseler, G. Braeuer, A. Waag, *Adv. Energy Mater.* **2019**, *9*, 1900725.

[42] Z. Li, S. Wang, J. Wu, W. Zhou, *Renewable Sustainable Energy Rev.* **2022**, *156*, 111980.

[43] L. N. Costa, F. X. Nobre, A. O. Lobo, J. M. E. de Matos, *Environ. Nanotechnol. Monit. Manage.* **2021**, *16*, 100466.

[44] P. Kubelka, F. Munk, *Z. Tech. Phys.* **1931**, *12*, 593.

[45] P. Makuła, M. Pacia, W. Macyk, *J. Phys. Chem. Lett.* **2018**, *9*, 6814.

[46] S. Stoll, A. Schweiger, *J. Magn. Reson.* **2006**, *178*, 42.

2212486 (10 of 10)